TB44

19th International Symposium of Ballistics, 7–11 May 2001, Interlaken, Switzerland

FRAGMENT IMPACT ON BI-LAYERED LIGHT ARMOURS EXPERIMENTAL ANALYSIS, MATERIAL MODELING AND NUMERICAL STUDIES

W. Riedel*, E. Straßburger, B. Lexow, H. Nahme, K. Thoma

Fraunhofer-Institut für Kurzzeitdynamik, Ernst-Mach-Institut (EMI), Eckerstr. 4, D-79104 Freiburg

Layered armour designs combining front plates with high shearing strength and deformable liner materials to catch debris or projectile fragments have been to be specially weight effective. The understanding of the underlying synergistic effects is necessary for effective armour designs. In this paper the component high hardness steel and aramid cloth are separately characterised in specific material tests at high strain rates. From these tests input data is derived for constitutive models which is employed in hydrocode simulations of impacts on bi-layered lightweight armours. Steel cylinders (L/D=0.8, 25 g) impacting at 900 to 1300 m/s are considered. The reproduction of the experimental results is discussed and synergistic effects are analysed.

INTRODUCTION

Cost and weight effective light armours are used for protection against high velocity fragments and AP ammunitions. Their performance strongly depends on the design in terms of plate construction and thickness. The considered experimental test program on the combined armour has been described in detail previously [1]. Thus, only the key information needed for validating the numerical simulations is given here. The bi-layered armour (see Fig. 1, left) consists of a front plate of hard armour steel XH129 (30 CrMo 25, Hardness 480–530 HB, Yield Limit $R_{p0,2}$= 1300 MPa, Ultimate Strength 1600 MPa). Plate thicknesses of 7.9 mm and 13.5 mm were chosen. The steel plate is backed by pressed laminates of 5, 10 or 21 layers (2.4 / 4.8 / 10 mm thickness) of neoprene coated aramid fabric. The lateral dimensions of the target are 200 x 200 mm, clamped in a massive rectangular steel frame with inner an inner opening of 150 x 150 mm. The projectiles are carbon steel C45 cylinders (aspect ratio of L/D = 0.8, D = 17.2 mm) simulating natural fragment impact. Flash X-ray radiographs and high-speed photography (see Fig. 2) are employed to determine residual projectile and fragment velocities and the time resolved deformation of the laminate. The protective performance is demonstrated by ballistic limit curves, e.g. plotting the normalised areal density ($\rho_{FTOT}=\rho_{FSTEEL}+\rho_{FLINER}$, normalised by the projectile diameter D) versus the projectile velocity (Fig. 1, right).

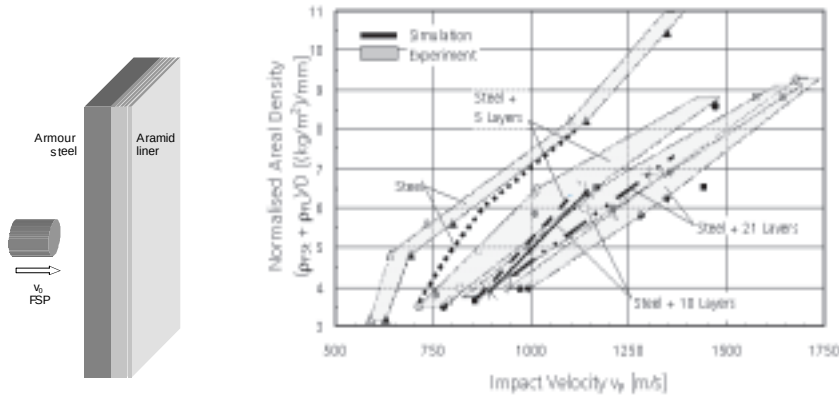

Figure 1: (left) experimental configuration; (right) ballsitic limit depending on ratio steel/liner.

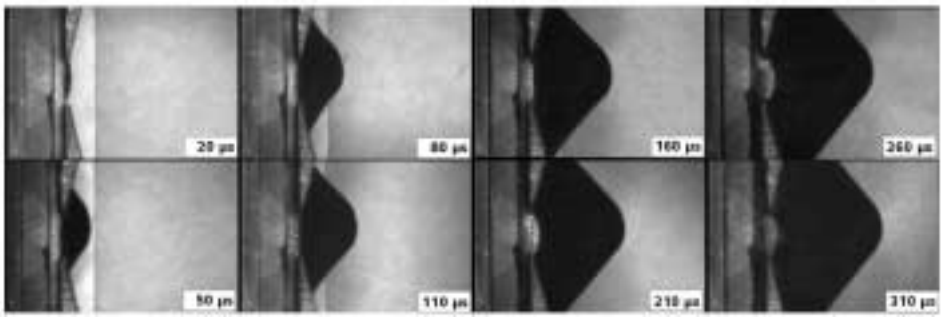

Figure 2: High speed photograph series of liner bulging; 13.5mm steel + 10 layers aramid, v_0=1255 m/s.

The protective role of the liner material is based on its deformability on a high level of tensile stresses. Significant performance is achieved when the liner is able to follow and thus decelerate the fragments forming a bulge of 30–60 mm depth (see Fig. 2). Overloading the liner in shear deformation results in failure already at low bulging deformation, before a significant tensile loading of the liner can occur.

CHARACTERISATION OF THE ARAMID CLOTH

The mechanical properties of aramid cloth were derived from an earlier experimental campaign on space protection shielding systems [2]. Measuring re-ordering processes of the weave and yarn stiffness (see Fig. 3, left), uniaxial tensile tests do not characterise primary mechanical properties of cloth materials. Loading conditions similar to the bulge formation are induced by a specialised biaxial test method for cloth material developed by Nahme et al. [3]. A circular sheet (initial radius ρ) is fixed at the end of a shock tube (see

Fig. 3, right). An increasing pressure in the tube will expand the weave to a spherical shape. The deflection of the sample centre h is recorded by a high-speed camera placed parallel to the weave. The displacement can be deduced from camera recordings according to the pixel and the time resolution.

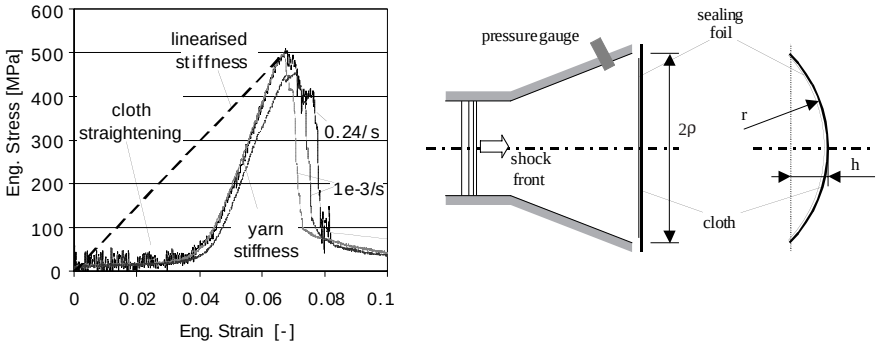

Figure 3: (Left) Unixial test results; (Right) Biaxial test configuration for cloth samples.

Radial strains ε_{rr} and hoop strains ε_{tt} are calculated by simple geometric considerations from the height h of the bulge (1a). As derived in [2] the stresses in the weave are calculated via the spherical vessel formula depending on the overpressure p by eq. (1,b). d denotes the thickness of the cloth.

$$\varepsilon_{rr}(h)=\varepsilon_{tt}(h)=\frac{\rho^2+h^2}{2\rho h}\arctan\left(\frac{2\rho h}{\rho^2-h^2}\right)-1\;; \qquad \sigma_{rr}=\frac{p\cdot r}{2d} \qquad (1a,b)$$

In [2] numerous other material characterisation tests have been performed on aramid (confined compression test, gauged reactive confinement test, plate impact tests etc.). These are more relevant for the compression behaviour of the material when employed as front (attenuating) layer. Capabilities as catching liner materials were found to be mainly dominated by the tensile behaviour of the weave.

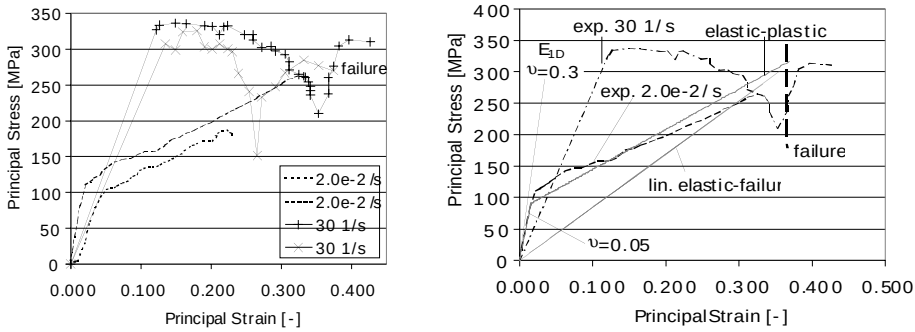

Figure 4: Measured (left) and modeled (right) static and dynamic biaxial stress-strain data for aramid.

MODELING APPROACHES FOR WOVEN CLOTH

The tested aramid cloth shows a symmetric 0°/90° weave pattern. Thus, orthotropic strength properties can be considered, e.g. with the through-thickness direction 1 and the two yarn directions 2 and 3. The stress-strain relationship is generally written as eq. (2). If the material symmetry axes 1,2,3 are parallel to the spatial coordinates x,y,z the linear elastic stiffness matrix [C] is given by eq. (3a).

$$\{\varepsilon\} = [C]\{\sigma\} \text{ with } \langle\sigma\rangle = \langle \sigma_{xx} \quad \sigma_{yy} \quad \sigma_{zz} \quad \sigma_{xy} \quad \sigma_{xz} \quad \sigma_{yz} \rangle, \ \langle\varepsilon\rangle = \langle \varepsilon_{xx} \ldots \rangle \qquad (2)$$

general orthotropic

$$[C] = \begin{bmatrix} \frac{1}{E_1} & \frac{-\upsilon_{21}}{E_2} & \frac{-\upsilon_{31}}{E_3} & 0 & 0 & 0 \\ \frac{-\upsilon_{12}}{E_1} & \frac{1}{E_2} & \frac{-\upsilon_{32}}{E_3} & 0 & 0 & 0 \\ \frac{-\upsilon_{13}}{E_1} & \frac{-\upsilon_{23}}{E_2} & \frac{1}{E_3} & 0 & 0 & 0 \\ 0 & 0 & 0 & \frac{1}{G_{12}} & 0 & 0 \\ 0 & 0 & 0 & 0 & \frac{1}{G_{13}} & 0 \\ 0 & 0 & 0 & 0 & 0 & \frac{1}{G_{23}} \end{bmatrix}$$

transverse isotropic (2–3 plane)

$$[C] = \begin{bmatrix} \frac{1}{E_1} & \frac{-\upsilon_{12}}{E_1} & \frac{-\upsilon_{12}}{E_1} & 0 & 0 & 0 \\ \frac{-\upsilon_{12}}{E_1} & \frac{1}{E_2} & \frac{-\upsilon_{23}}{E_2} & 0 & 0 & 0 \\ \frac{-\upsilon_{12}}{E_1} & \frac{-\upsilon_{23}}{E_2} & \frac{1}{E_2} & 0 & 0 & 0 \\ 0 & 0 & 0 & \frac{1}{G_{12}} & 0 & 0 \\ 0 & 0 & 0 & 0 & \frac{1}{G_{12}} & 0 \\ 0 & 0 & 0 & 0 & 0 & \frac{2(1+\upsilon_{23})}{G_{23}} \end{bmatrix} \qquad (3a,b)$$

During uniaxial testing no important difference was noticed among the in-plane stiffnesses E_2 and E_3. Furthermore, the weave formed spherical bulk sections under biaxial tension. A description as transverse isotropic material with respect to the weave plane seems therefore justified.

E_2=E_3 being defined, the in-plane Poisson effect has to be quantified by υ_{23} or G_{23}. It can be derived by comparing uniaxial and biaxial stiffnesses. A linearised uniaxial tensile stiffness was used as starting point (see Fig. 3, left). The Poisson effect contributes to the biaxial stiffness as in eq. (4a). This influence is plotted in Fig. 4, right, for the values for an example value of υ_{23}=0.3. The best agreement with the initial slope in the tests was obtained specifying υ_{23}=0.05.

$$E = \frac{\sigma_I}{\varepsilon_I}\frac{1-\upsilon^2}{1+\upsilon} \qquad \varepsilon_{eff} = \frac{2}{3}\left[\left(\varepsilon_1^2+\varepsilon_2^2+\varepsilon_3^2\right)+5\left(\varepsilon_1\varepsilon_2+\varepsilon_2\varepsilon_3+\varepsilon_1\varepsilon_3\right)-3\varepsilon_{12}\right]^{1/2} \qquad (4a,b)$$

Two approaches where chosen to reproduce the slope of the biaxial stress-strain curve up to failure:

1) Plastic hardening above 90 Mpa: Tangent Modulus E_T=45 MPa, (E_{elast}=5.5 GPa, υ=0.05)
2) Reduced overall elastic stiffness up to failure (E_{elast}=593 MPa, υ=0.3).

Both resulting stress-strain curves are compared in Fig. 4, right, to the experimental data. Failure is activated at ε_{eff}=65% effective strain (4b) in agreement with the ultimate deformations in the biaxial tension test.

So far, only components of the stiffness matrix describing membrane stresses (bold components in eq. (3b) are considered. Representing the liner layers by plane stress shell elements, all components containing E1 are neglected. Through thickness stresses are exclusively handled by the contact algorithm. Nevertheless, bending moments can be considered through the shear modulus G_{12}. Having no experimental data available on this property, a parametric approach was used to study the influence in the ballistic application. G_{12} was chosen for $\upsilon_{12}=\upsilon_{23}$ as an upper bond. In the simulations described below the resulting bending moments showed no effect on the phenomenology and the efficiency of the armour.

CHARACTERISATION OF THE ARMOUR STEEL

The steel material of the front armour plate was characterised following an integral characterisation procedure recently proposed by Rohr et al. [4,5]. Ultrasonic measurements specified the longitudinal sound speed to c_P = 5880 m/s (plane strain). Quasistatic tensile properties at strain rates of 10^{-3} 1/s were taken from material specification sheets. Taylor tests with VISAR interferometry provided the dynamic yield strength, hardening and failure properties at strain rates of 3000 1/s. Equation of state properties, the Hugoniot elastic limit and spall strength at strain rates up to 10^6 1/s were determined form plate impact tests. The yield limit over nine decades of strain rates is one key result of this characterisation procedure. Fig. 5 shows no significant strain rate sensitivity of the XH129 armour steel with respect to the yield points. The data for a softer HZB-L armour steel exhibiting strong strain rate dependence is given for comparison purposes. The measurements provided input data to constitutive models (see Table 1).

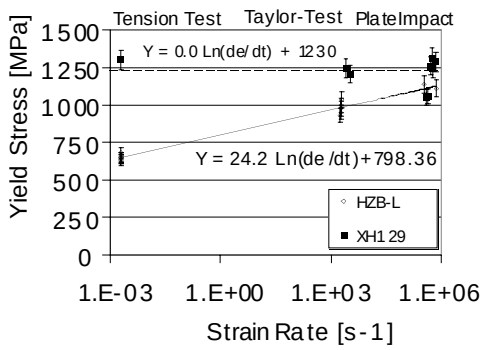

Figure 5: Strain rate sensitivity of the front plate armour steel in comparison to a softer quality [4,5].

Table 1: Derived material data for the amour steel layer (XH129)

Equation of State Mie-Grüneisen / Shock		**Strength Johnson, Cook [6]**	
ρ g/cm^3]	7.81	G [GPa]	81.0
Γ [-]	1.93	A [GPa]	1.3
c_B [m/s]	5044	B [MPa]	753.4
S [-]	0.3238	n [-]	0.42
T_{ref} [K]	300	C [-]	0
c_v [J/kgK]	420	m [-]	0.822
Failure		T_{melt} [K]	1800
$\sigma_{fail,11}$ [GPa]	10	$\varepsilon_{fail,11}$ [-]	0.65
$\sigma_{fail,22}$ [GPa]	5	$\varepsilon_{fail,12}$ [-]	0.5

NUMERICAL SIMULATION OF THE LIGHT ARMOUR EFFICIENCY

The material data described above forms the basis for finite element simulations with explicit time integration of the composed armour structure. The commercial hydrocode AUTODYN-2D and 3D [7] was used for all simulations shown below. A cell length of one millimeter is chosen for all components. The liner layers are modeled explicitly by shell elements (plane stress). The 'master-slave' contact algorithm with Coulomb friction of 7% handles the interaction in the penetration zone. Erosion at strains shortly above the failure strains describes the tunnelling process.

Rigid boundary conditions are applied to the steel and the aramid layers as in the experiment. The transition from penetration to perforation happens at early stages (before 200 µs, see Fig. 6, right) when the edges of the plate have not yet interfered. Consequently, axisymmetric calculations can be used for the ballistic limit analysis.

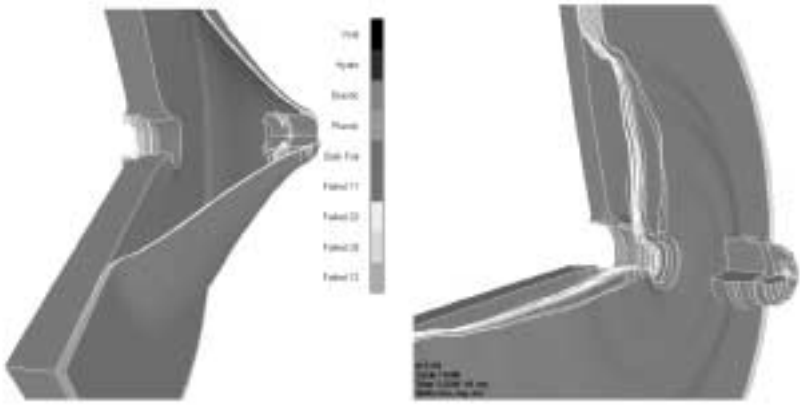

Figure 6: Liner catching the projectile (left, 3.25 ms, 5 layers), Perforation (right, 3.25 ms, 21 layers); Steel plate failure mechanisms, plug formation, projectile erosion and fragment deceleration by the liner.

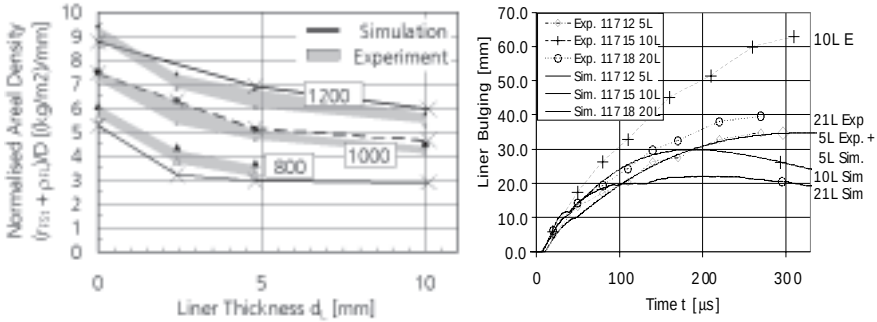

Figure 7: (Left) Liner effect on limit areal density; (Right) Liner bulging in experiment and simulation.

Plugging of the steel target plate and the erosion of the blunt projectile are qualitatively reproduced in the simulations (see Fig. 6). Although local spallation occurs, the dominant failure mechanism is excessive shearing. The formation of ring fragments at higher velocities [1] is underpredicted. Meshless techniques might allow to simulate the separation from the surrounding plate without mass losses from numerical erosion. Nevertheless, the ballistic limit of the monolayer steel target is calculated in good agreement with the experiments (see Fig. 7, left, liner thickness = 0).

The ballistic limits of bi-layered configurations are generally well reproduced, ranging from 7.9 to 13.5 mm steel and 5 to 21 layers of aramid weave (2.4 to 10 mm). Plotting in Fig. 7, left, the areal weights for ballistic limit velocities from 800 to 1200 m/s over the different thickness demonstrates the qualitative and quantitative protection effect. Yet, the time resolved liner deformation is underpredicted. Fig. 7, right, shows the experimental bulging height only correctly calculated for 5 liner layers.

SUMMARY AND PERSPECTIVES

Design assessment by numerical methods of light weight armours consisting of metallic front plates and cloth liner is generally possible. Precondition is a thorough characterisation of the component materials by well defined high strain rate experiments. Methodologies for metallic materials were demonstrated earlier [4,5] and applied to derive model parameters for the front armour material. Improvements are possible with respect to the formation of ring fragments.

Employing the large data base of different test types on aramid weave [2], the biaxial tension test turned out to be the most important characterisation experiment for woven liners. Assuming transverse isotropy, simple linear elastic and elastic-plastic hardening models together with strain failure criteria were chosen in the study. The application to the complete armour configuration proved to well reproduce the ballistic limits over a wide range of configurations. Discrepancies were noticed comparing the liner bulges close to the ballistic limit and should be studied in future analysis.

REFERENCES

1. E. Straßburger, H. Senf, H. Rothenhäusler, B. Lexow, R. Jeanquartier, 17th ISB, The Ballistic Resistance of Steel/Aramid Bi-Layer Amor against Fragment Impact, 1998
2. S. Hiermaier, W.Riedel, C.Hayhurst, R.Clegg, C. Wentzel, Advanced Material Models for Hypervelocity Impact Simulations, Final Report, EMI-Report E 43/98
3. Einrichtung zur Messung der dynamischen Gas- und insbesondere Luftdurchlässigkeit von Geweben, Patent Nr. 4407224, Deutsches Patentamt München, 1995
4. I. Rohr, Ermittlung von statischen und dynamischen Modellparametern für HZB996(L) am Beispiel des Johnson-Cook-Modells, EMI-Report E 64/00
5. I. Rohr, H. Nahme, W. Riedel, K. Thoma, Determination of static and dynamic model parameters for a German armor steel, to be published in Int. J. Imp. Engn.
6. Johnson, G.R., Cook W.H.: A Constitutive Model and Data for Metals Subjected to Large Strains, High Strain Rates and High Temperatures. Proc. 7th Int. Symposium on Ballistics, Den Haag, 1983 S. 81.–1ff
7. AUTODYN, Theory Manual, Century Dynamics Ltd. Horsham, United Kingdom, 2000